

Notice: This manuscript has been authored by UT-Battelle, LLC, under Contract No. DE-AC0500OR22725 with the U.S. Department of Energy. The United States Government retains and the publisher, by accepting the article for publication, acknowledges that the United States Government retains a non-exclusive, paid-up, irrevocable, world-wide license to publish or reproduce the published form of this manuscript, or allow others to do so, for the United States Government purposes. The Department of Energy will provide public access to these results of federally sponsored research in accordance with the DOE Public Access Plan (<http://energy.gov/downloads/doe-public-access-plan>).

Interplay between Topological States and Rashba States as Manifested on Surface Steps at Room Temperature

Wonhee Ko^{1,3†}, Seoung-Hun Kang^{2†}, Jason Lapano², Hao Chang^{1,3}, Jacob Teeter¹, Hoyeon Jeon¹,
Matthew Brahlek², Mina Yoon^{2*}, Robert G. Moore^{2*}, An-Ping Li^{1,3*}

¹*Center for Nanophase Materials Sciences, Oak Ridge National Laboratory, Oak Ridge, Tennessee
37831, USA*

²*Materials Science and Technology Division, Oak Ridge National Laboratory, Oak Ridge, Tennessee
37831, USA*

³*Department of Physics and Astronomy, The University of Tennessee, Knoxville, Tennessee 37996, USA*

†These authors contributed equally to this work

Email: myoon@ornl.gov, moorerg@ornl.gov, apli@ornl.gov

Abstract

The unique spin texture of quantum states in topological materials underpins many proposed spintronic applications. However, realizations of such great potential are stymied by perturbations, such as temperature and local fields imposed by impurities and defects, that can render a promising quantum state uncontrollable. Here, we report room-temperature observation of interaction between Rashba states and topological surface states, which manifests unique spin textures controllable by layer thickness of thin films. Specifically, we combine scanning tunneling microscopy/spectroscopy with the first-principles theoretical calculation to find the robust Rashba states coexisting with topological surface states along the surface steps with characteristic spin textures in momentum space. The Rashba edge states can be switched off by reducing the thickness of a topological insulator Bi_2Se_3 to bolster their interaction with the hybridized

topological surface states. The study unveils a manipulating mechanism of the spin textures at room temperature, reinforcing the necessity of thin film technology in controlling quantum states.

Keywords

Topological insulators, Bi₂Se₃ film, Topological surface states, Rashba edge states, Scanning tunneling microscopy, First-principles density functional theory, Tight-binding modeling

In topological materials with large spin-orbit coupling, several quantum states possess unique spin texture to be useful for spintronic functionality. For example, in three-dimensional (3D) quantum spin Hall insulators (i.e. topological insulators), topological surface states exhibit spin-momentum locking [1,2] which allows conversion of charge current to spin polarization [3,4] or vice versa [5,6]. Topological insulators also host Rashba states on the surface caused by inversion symmetry breaking and quantum confinement [7,8], although topologically trivial, whose spin texture induces spin-charge conversion through Rashba-Edelstein effect [9,10]. The joint effect of the two spin-related interactions can lead to complex spin and charge transport phenomena that remain to be evaluated [11].

The spintronic functionality, however, of the topological insulator-based devices has been mostly demonstrated at the cryogenic temperature [4,12-16]. One reason is that even though the quantum states are protected by non-trivial topology and manifested themselves at room temperature [7,17-19], their electronic properties are significantly hampered by external perturbations, such as unintentional doping, thermally excited bulk carriers, and intrinsic defects [20-25]. A representative example of such deterioration is quantum transport in MnBi₂Te₄, where the combined magnetism and non-trivial topology are expected to result in ballistic spin transport by quantum anomalous Hall effect at relatively high temperature [26-28], but its experimental realization is still controversial [29-32]. Moreover, manipulating these quantum states involves the interaction in the energy scale of typically order of magnitude less than the state itself [9,33],

further restricting the demonstration of any device functionality at ambient condition. To achieve practical spintronic devices with topological materials, it is critical to realize robust quantum states with spin texture and well-defined interaction.

In this study, we show that the surface steps of topological insulators create robust Rashba edge states and demonstrate their interactions with the topological surface states, all at room temperature. Specifically, we investigated Bi_2Se_3 thin film with precisely tuned nominal thickness and used scanning tunneling microscopy/spectroscopy (STM/S) to identify the single quintuple layer (QL) steps and characterize their electronic structure [Fig. 1(a)]. For the films thicker than critical QL thickness N_c , steps induce translational symmetry breaking, giving rise to the Rashba edge states that are detected as the enhanced differential tunneling conductance localized along the steps at around Dirac point E_D . The Rashba edge states are robust against edge geometry and dislocations, and persist up to the room temperature. However, the edge states disappear in STM/S when the film thickness becomes less than N_c QL, where $N_c = 7\sim 9$. The first-principles density functional theory (DFT) calculations confirm the coexistence of topological surface states and Rashba edge states at the surface steps with distinct band dispersion and spin texture for the films thicker than 5 QL. Furthermore, theoretical calculations show that the top and bottom topological surface states start to hybridize and overlap significantly with the Rashba edge states when the film thickness is reduced below 5 QL, whose value is close to the N_c from STM observation, and as a result, the edge states become delocalized across the surface. The observation is an unambiguous demonstration of the interaction between the topological and Rashba states at room temperature.

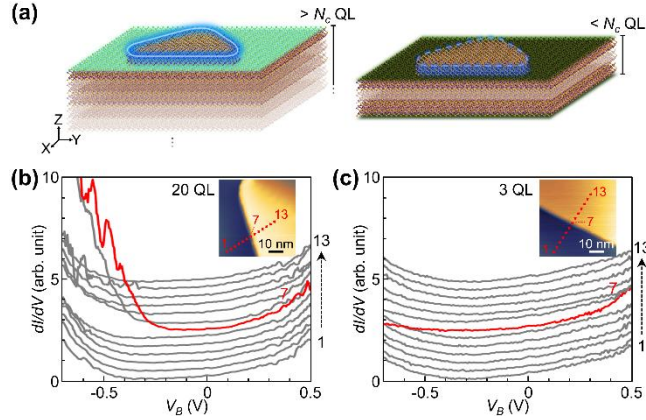


FIG. 1. Rashba edge states in Bi₂Se₃ film and its interplay with topological surface states. (a) Schematic of the interplay between Rashba edge states and topological surface states for the films thicker than critical QL thickness N_c (right) and thinner than N_c (left). In the thick film ($> N_c$ QL), bright green surface and blue line indicates topological surface states and Rashba edge states, respectively. However, in the thin film ($< N_c$ QL), the topological surface states open the gap (dark green surface), and edge states disappear (dotted blue line). (b,c) dI/dV spectra across the step taken on 20 QL film and 3 QL film, respectively. Inset of (b) and (c) shows the topographic image of the film ($V_B = 1$ V, $I = 1$ pA for (b); $V_B = 1$ V, $I = 2$ pA for (c)). The locations of spectra are marked by red dots and numbers on the topographic images.

To characterize the edge states and observe their interaction with topological surface states, we took the dI/dV spectra across the single QL steps in the Bi₂Se₃ thin films with varying thicknesses. Specifically, 20 QL and 3 QL films were investigated to compare the behavior of edge states for thickness above and below the critical thickness of 5 QL, which was reported as the thickness that starts to open the band gap at the Dirac point by hybridization of the top and bottom surface states [34]. The ARPES measurement confirmed that 20 QL film retains the crossing of bands at the Dirac point of topological surface states, while 3 QL film displays the clear band gap opening at the Dirac point [Fig. S1] [35]. The large- and atomic-scale STM images of both films display atomically flat surface with a few single QL step edges [Fig. S2]. In Fig. 1(b)

and (c), we compare dI/dV spectra across the single QL step edges on the films with a nominal thickness of 20 QL and 3 QL, respectively. At the terraces far from the edges, the dI/dV spectra of both films display a similar dip shape with the minimum at about -0.3 eV, which is consistent with the existence of the surface states with Dirac point $E_D \sim -0.3$ eV in Bi_2Se_3 [36,37]. However, when the tip is placed right on top of the step, dI/dV spectra (red curve) from the 20 QL sample exhibit a significant enhancement of intensity below E_D . Such an increase indicates the existence of the edge states localized along the physical step for energy from E_D to the bulk valence band, which was previously predicted and observed on topological insulators [38-40]. In striking contrast, the dI/dV spectra from the 3 QL sample do not show any enhancement in the energy range of -0.7 ~ 0.3 eV across the step edge, and the spectrum right above the step edge even displays a slight decrease in the intensity below E_D . The results strongly indicate that the signature of the edge states disappears when the film thickness is reduced to 3 QL. Further measurement of films with various thicknesses, different substrates, and temperatures of 4.6 K and room temperatures, consistently exhibited the disappearance of edge states below 6 QL and appearance of edge states above 10 QL [Fig. S3].

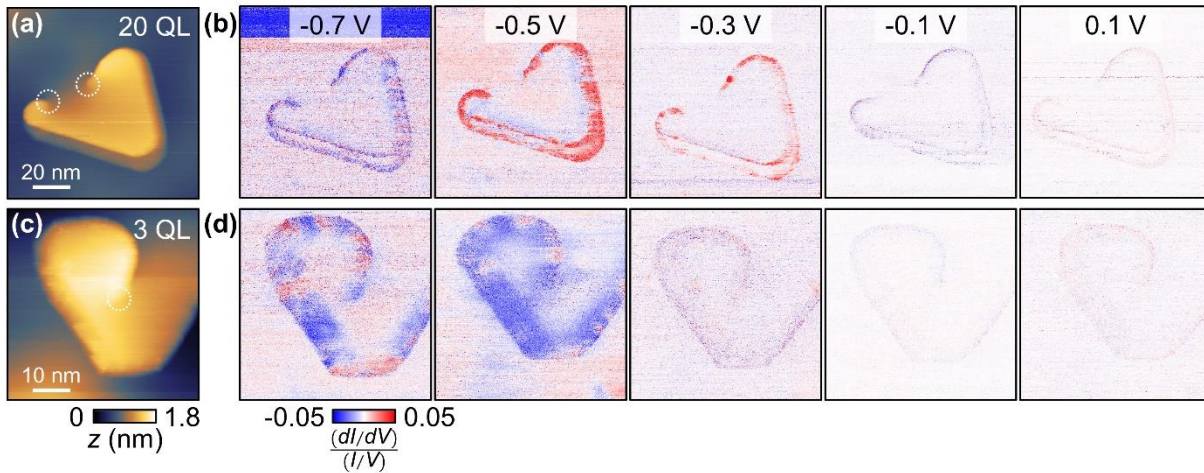


FIG. 2. Normalized dI/dV maps of a single QL steps on the 20 QL and 3QL samples. (a) A topographic image of single QL step on 20 QL film. ($V_B = 0.3$ V, $I = 100$ pA). Dotted circles denote the screw dislocations. (b) Normalized dI/dV maps taken at the same area of (a) for different bias voltages. (c) A

topographic image of single QL step on 3 QL film ($V_B = -0.7$ V, $I = 100$ pA). Dotted circles denote the screw dislocations. (d) Normalized dI/dV maps taken at the same area of (c) for different bias voltages.

To investigate the spatial distribution of the edge states and their dependence on the film thickness, we measured dI/dV maps at the region with single QL steps for 20 QL and 3 QL films [Fig. 2]. To remove the artifacts in dI/dV maps from the fluctuation of current, we normalized dI/dV by dividing it with I/V [Fig. S4] [35]. When $E > E_D$, there is little contrast along the edges for both 20 QL and 3 QL films, indicating that no edge states exist in this energy range. However, for 20 QL film, dI/dV maps at the E_D and below ($-0.5 \sim -0.3$ eV) show significant enhancement of intensity along the step edge [Fig. 2(b)]. This confirms the existence of edge states that are tightly localized at the physical step, which is consistent with the observation in Fig. 1(b) that displays the new states below E_D for dI/dV spectra at the edge. Moreover, the dI/dV maps show that the edge states are robust against the geometrical disorders, as they persist over the curves and screw dislocations in the step edge. The dI/dV maps on 3 QL film, however, display drastically different features. For all energies, including E_D , dI/dV along the step edges do not show discernable enhancement [Fig. 2(d)]. At E_D and below ($-0.5 \sim -0.3$ eV), dI/dV signal displayed slight depression in contrast. No appearance of enhanced dI/dV along the step edge verifies that the edge states have disappeared for the 3 QL film. When the energy reaches deep inside the bulk valence band (-0.7 eV), both 20 QL and 3 QL films exhibit a similar pattern of depression along the edges. The observation indicates that the disappearance of the edge state signal is most likely related to the topological surface states.

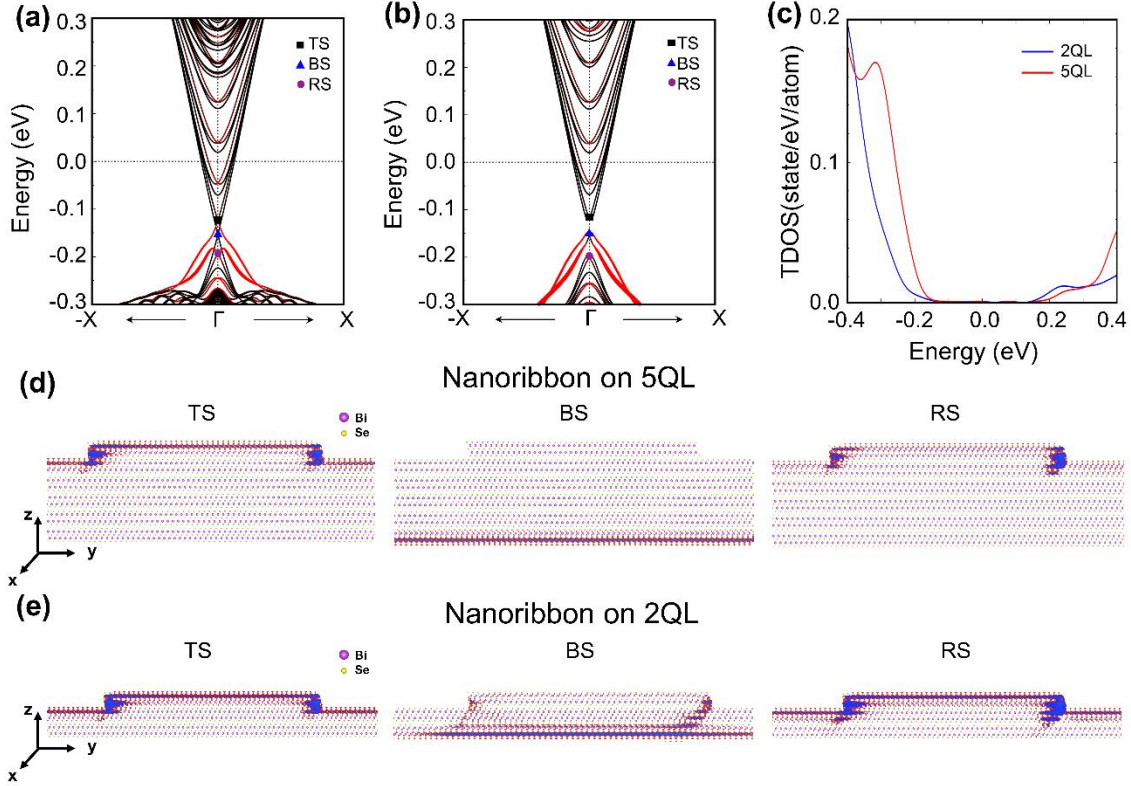


FIG. 3. Theoretical electronic structures of nanoribbon on thick (5QL) and thin (2QL) layers. (a) Band structure for nanoribbon on thick and (b), thin layers. The red color is proportional to the band projection at the step edge. (c) Total density of states of nanoribbon on thick (red line) and thin (blue line) layers. (d) Charge density at the gamma for top, bottom surface states (TS, BS), and Rashba states (RS) denoted by a black square, blue triangle, and purple circle dots in (a), respectively. (e) Charge density at the gamma for TS, BS, and RS denoted by a black square, blue triangle, and purple circle dots in (b), respectively.

To understand the origins of localized edge states and their thickness dependence, we investigated the topological surface states of Bi_2Se_3 according to the film thickness using the reliable tight-binding parameters of Bi_2Se_3 . To confirm the strength of crosstalk between the top and bottom topological surface states, we checked the band gap as the function of thickness. As the film thickness increases from 1 QL, the band gap gradually decreases until the band crossing at the Dirac point is confirmed in 5 QL [Fig. S5]

[34,35]. Experimentally, the strength of crosstalk between the top and bottom topological surfaces can be estimated by the band gap measured by ARPES. The band gap of 3 QL film is about 100 meV [Fig. S1(b)] [35], which is in good agreement with 2 QL in our simulation [Figs. S5(c) and (d)] [35]. Therefore, we compare the thick (20 QL) and thin (3 QL) film case of the experiment to the electronic structure simulation of the nanoribbons on 5 QL and 2QL films. Figure 3(a) shows the additional states localized at the step edge in the 5 QL film. The pristine topological insulator without any step edge should present the Dirac point with a degenerated linear dispersion from both the top and bottom surface states around E_D . However, since the step breaks the inversion symmetry, the bands of top and bottom Dirac states become split, and 1D localized edge states are formed, as shown in Figs. 3(a) and (d). The 1D localized edge states are the type-1 Rashba state, i.e., one possesses a momentum-dependent splitting of the spin band induced by strong spin-orbit coupling (SOC) and asymmetric potential [Fig. S7] [35]. Further calculation of 10 QL film displays the same 1D Rashba states although the bulk states change [Fig. S10]. The energy and spatial distribution of the 1D Rashba states in Figs. 3(a) and (d) are consistent with the edge states observed in the dI/dV maps of 20 QL film in Fig. 2(b).

We further confirmed the robustness of Rashba states against variations in step edge shapes by conducting a comprehensive tight-binding study on various edge configurations [Fig. S8, S9 and Table S2]. Our results revealed that, under the Se-rich condition of our MBE synthesis, all edge terminations including ziazag, armchair, and triangular types harbor the Rashba edge states with a substantial Rashba strength. We also note that although some topological materials display topological edge states in 2D limit [41,42], the observed edge states cannot be topological since our theoretical topological index (Z_2) calculation shows that Bi_2Se_3 films have trivial topology ($Z_2 = 0$) up to 8 QL.

In contrast, the thin film (2 QL) does not form localized 1D Rashba state and band crossing around E_D [Fig. 3(b)]. Instead, both top surface states and Rashba states from the nanoribbon edges interact with bottom surface state, resulting in coupled and gapped states as shown in Figs. 3(b) and (e). So, the coupling between Rashba states and bottom surface states render delocalized hybridized states, as shown in Fig. 3(e), which explains the disappearance of dI/dV features from the edge states for 3QL film in Fig. 2(d). We note

that the interaction between Rashba state and top surface states does not appear near the gamma point due to the different energy levels as shown in Figs. 3(a) and (b). The calculation also confirms the difference in the total density of states below the -0.2 eV in Fig. 3(c), which agrees with the thickness-dependent appearance of a peak below E_D in dI/dV spectra at the edge [Figs. 1(b) and (c)]. Therefore, our theoretical simulations agree well with the experimental observations.

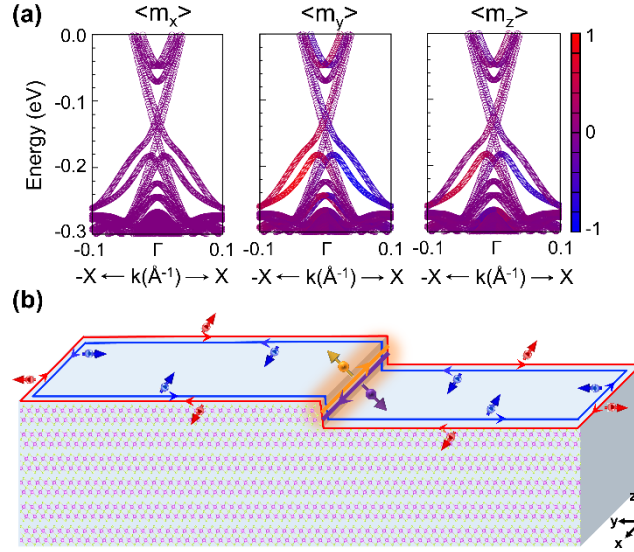


FIG. 4. Spin orientation of electronic bands in nanoribbon on thick (5 QL) layer. (a) Color coded band structures in which the expectation values of spin along x , y , z directions for edge atoms in the top nanoribbon layer. Red and blue correspond to the \pm spin direction for the x , y , and z -axis. (b) Schematic spin orientation for top surface state and 1D Rashba state in real space. The red and blue lines (arrows) represent the topological surface states (spin direction). Orange and purple lines (arrows) correspond to the 1D Rashba state (spin direction).

We now evaluate the spin orientation of the Rashba state and top surface state for the thick film using the spin projection in band structures, as shown in Fig. 4(a). The spin orientation of Rashba states at step edge is $\pm yz$ -direction for the $\mp x$ -momentum directions [Fig. 4(b)], while the top topological surface state is $\pm y$ -direction for the $\mp x$ -momentum directions. We confirm that both states have a spin-momentum

locking with spin locked orthogonally to the momentum direction, which is a key common feature of the Rashba state and topological surface states. Their spins, however, are not parallel for the same momentum directions so that they can exist at the same energy level without any additional crystal symmetry. Even if the step makes a terrace discontinuous, the topological top surface state is continuous across the step and coexists with the 1D Rashba states at the step edge. Electrons at the edge can have four spin polarized states with $+y$, $-y$, $+xy$, and $-xy$ spin directions at the same energy level.

In summary, we have revealed the interaction between the Rashba edge states and topological surface states in the Bi_2Se_3 thin films with different thicknesses. The edge states are clearly observed as enhanced dI/dV localized along the step edges in 20 QL film, however, the edge states signal completely disappears when the film thickness is reduced to 3 QL. Theoretical calculations reveal that the thick film supports 1D Rashba states along the step edge, but if the film thickness decreases below 5 QL, then the charge density of Rashba states significantly overlaps with bottom surface states and becomes largely diffused by the interaction between them. Both topological surface states and Rashba states possess spin textures associated with their chiral edge conductance, thus preventing electron backscattering and generating robust spin currents. The induced spins by these two mechanisms are unparallel, though both are perpendicularly locked to the same wave vectors. The demonstration of switching off the Rashba spin channel through interactions with topological states at room temperature provides a foundation for realizing novel spintronic devices. Moreover, since surface steps (more generally, inversion asymmetric structures) are ubiquitous and Rashba states form 1D channels along step edges for most of the topological materials with a strong spin-orbit coupling, our finding offers a new route for designing topological spintronics devices based on inversion asymmetric structures for topological materials. For example, it is expected that the Rashba spin-orbit coupling allows for tuning the position of the zero energy crossings in the flux parameter space and has sizable effects on spin-polarized persistent currents in a topological superconducting nanowire [43]. Thus, the controllable interaction between Rashba states and topological surface states provides an excellent means toward exotic quantum phenomena and topological quantum devices [44,45].

Acknowledgement

This work was supported by the U.S. DOE, Office of Science, National Quantum Information Science Research Centers, Quantum Science Center (S.H.K, R.G.M., A.-P.L.), and by the US Department of Energy, Office of Science, Office of Basic Energy Sciences, Materials Sciences and Engineering Division (J.L., M.B., M.Y.). This research used resources of the Oak Ridge Leadership Computing Facility and the National Energy Research Scientific Computing Center, US Department of Energy Office of Science User Facilities. The STM measurement was conducted at the Center for Nanophase Materials Sciences (CNMS), which is a US Department of Energy, Office of Science User Facility.

References

- [1] M. Z. Hasan and C. L. Kane, *Colloquium: Topological insulators*, Rev. Mod. Phys. **82**, 3045 (2010).
- [2] X. L. Qi and S. C. Zhang, *Topological insulators and superconductors*, Rev. Mod. Phys. **83**, 1057 (2011).
- [3] A. R. Mellnik, J. S. Lee, A. Richardella, J. L. Grab, P. J. Mintun, M. H. Fischer, A. Vaezi, A. Manchon, E. A. Kim, N. Samarth, and D. C. Ralph, *Spin-transfer torque generated by a topological insulator*, Nature **511**, 449 (2014).
- [4] C. H. Li, O. M. J. Van't Erve, J. T. Robinson, Y. Liu, L. Li, and B. T. Jonker, *Electrical detection of charge-current-induced spin polarization due to spin-momentum locking in Bi_2Se_3* , Nat. Nanotechnol. **9**, 218 (2014).
- [5] J. C. Rojas-Sánchez, S. Oyarzún, Y. Fu, A. Marty, C. Vergnaud, S. Gambarelli, L. Vila, M. Jamet, Y. Ohtsubo, A. Taleb-Ibrahimi, P. Le Fèvre, F. Bertran, N. Reyren, J. M. George, and A. Fert, *Spin to Charge Conversion at Room Temperature by Spin Pumping into a New Type of Topological Insulator: α -Sn Films*, Phys. Rev. Lett. **116**, 096602 (2016).
- [6] Y. Shiomi, K. Nomura, Y. Kajiwara, K. Eto, M. Novak, K. Segawa, Y. Ando, and E. Saitoh, *Spin-electricity conversion induced by spin injection into topological insulators*, Phys. Rev. Lett. **113**, 196601 (2014).
- [7] P. D. C. King, R. C. Hatch, M. Bianchi, R. Ovsyannikov, C. Lupulescu, G. Landolt, B. Slomski, J. H. Dil, D. Guan, J. L. Mi, E. D. L. Rienks, J. Fink, A. Lindblad, S. Svensson, S. Bao, G. Balakrishnan, B. B. Iversen, J. Osterwalder, W. Eberhardt, F. Baumberger, and P. Hofmann, *Large Tunable Rashba Spin Splitting of a Two-Dimensional Electron Gas in Bi_2Se_3* , Phys. Rev. Lett. **107**, 096802 (2011).
- [8] Z. H. Zhu, G. Levy, B. Ludbrook, C. N. Veenstra, J. A. Rosen, R. Comin, D. Wong, P. Dosanjh, A. Ubaldini, P. Syers, N. P. Butch, J. Paglione, I. S. Elfimov, and A. Damascelli, *Rashba spin-splitting control at the surface of the topological insulator Bi_2Se_3* , Phys. Rev. Lett. **107**, 186405 (2011).
- [9] V. M. Edelstein, *Spin polarization of conduction electrons induced by electric current in two-dimensional asymmetric electron systems*, Solid State Commun. **73**, 233 (1990).

- [10] J. C. R. Sánchez, L. Vila, G. Desfonds, S. Gambarelli, J. P. Attané, J. M. De Teresa, C. Magén, and A. Fert, *Spin-to-charge conversion using Rashba coupling at the interface between non-magnetic materials*, Nat. Commun. **4**, 2944 (2013).
- [11] J. Tian, C. Şahin, I. Miotkowski, M. E. Flatté, and Y. P. Chen, *Opposite current-induced spin polarizations in bulk-metallic Bi_2Se_3 and bulk-insulating $\text{Bi}_2\text{Te}_2\text{Se}$ topological insulator thin flakes*, Phys. Rev. B **103**, 035412 (2021).
- [12] Y. Ando, T. Hamasaki, T. Kurokawa, K. Ichiba, F. Yang, M. Novak, S. Sasaki, K. Segawa, Y. Ando, and M. Shiraishi, *Electrical detection of the spin polarization due to charge flow in the surface state of the topological insulator $\text{Bi}_{1.5}\text{Sb}_{0.5}\text{Te}_{1.7}\text{Se}_{1.3}$* , Nano Lett. **14**, 6226 (2014).
- [13] J. S. Lee, A. Richardella, D. R. Hickey, K. A. Mkhoyan, and N. Samarth, *Mapping the chemical potential dependence of current-induced spin polarization in a topological insulator*, Phys. Rev. B **92**, 155312 (2015).
- [14] J. Tian, I. Miotkowski, S. Hong, and Y. P. Chen, *Electrical injection and detection of spin-polarized currents in topological insulator $\text{Bi}_2\text{Te}_2\text{Se}$* , Sci. Rep. **5**, 14293 (2015).
- [15] S. M. Hus, X. G. Zhang, G. D. Nguyen, W. Ko, A. P. Baddorf, Y. P. Chen, and A.-P. Li, *Detection of the Spin-Chemical Potential in Topological Insulators Using Spin-Polarized Four-Probe STM*, Phys. Rev. Lett. **119**, 137202 (2017).
- [16] W. Ko, G. D. Nguyen, H. Kim, J. S. Kim, X. G. Zhang, and A.-P. Li, *Accessing the Intrinsic Spin Transport in a Topological Insulator by Controlling the Crossover of Bulk-to-Surface Conductance*, Phys. Rev. Lett. **121**, 176801 (2018).
- [17] R. C. Hatch, M. Bianchi, D. Guan, S. Bao, J. Mi, B. B. Iversen, L. Nilsson, L. Hornekær, and P. Hofmann, *Stability of the $\text{Bi}_2\text{Se}_3(111)$ topological state: Electron-phonon and electron-defect scattering*, Phys. Rev. B **83**, 241303(R) (2011).
- [18] Z. H. Pan, A. V. Fedorov, D. Gardner, Y. S. Lee, S. Chu, and T. Valla, *Measurement of an exceptionally weak electron-phonon coupling on the surface of the topological insulator Bi_2Se_3 using angle-resolved photoemission spectroscopy*, Phys. Rev. Lett. **108**, 187001 (2012).
- [19] Z. H. Pan, E. Vescovo, A. V. Fedorov, G. D. Gu, and T. Valla, *Persistent coherence and spin polarization of topological surface states on topological insulators*, Phys. Rev. B **88**, 041101(R) (2013).
- [20] Y. Ando, *Topological insulator materials*, J. Phys. Soc. Japan **82**, 102001 (2013).
- [21] J. G. Analytis, R. D. McDonald, S. C. Riggs, J. H. Chu, G. S. Boebinger, and I. R. Fisher, *Two-dimensional surface state in the quantum limit of a topological insulator*, Nat. Phys. **6**, 960 (2010).
- [22] N. Koirala, M. Brahlek, M. Salehi, L. Wu, J. Dai, J. Waugh, T. Nummy, M. G. Han, J. Moon, Y. Zhu, D. Dessau, W. Wu, N. P. Armitage, and S. Oh, *Record Surface State Mobility and Quantum Hall Effect in Topological Insulator Thin Films via Interface Engineering*, Nano Lett. **15**, 8245 (2015).
- [23] Y. Xu, J. Chiu, L. Miao, H. He, Z. Alpichshev, A. Kapitulnik, R. R. Biswas, and L. A. Wray, *Disorder enabled band structure engineering of a topological insulator surface*, Nat. Commun. **8**, 14081 (2017).
- [24] L. Miao, Y. Xu, W. Zhang, D. Older, S. A. Breitweiser, E. Kotta, H. He, T. Suzuki, J. D. Denlinger, R. R. Biswas, J. G. Checkelsky, W. Wu, and L. A. Wray, *Observation of a topological insulator Dirac cone reshaped by non-magnetic impurity resonance*, npj Quantum Mater. **3**, 101 (2018).
- [25] E. Kotta, L. Miao, Y. Xu, S. Alexander Breitweiser, C. Jozwiak, A. Bostwick, E. Rotenberg, W. Zhang, W. Wu, T. Suzuki, J. Checkelsky, and L. Andrew Wray, *Spectromicroscopic measurement of surface and bulk band structure interplay in a disordered topological insulator*, Nat. Phys. **16**, 285 (2020).
- [26] J. Li, Y. Li, S. Du, Z. Wang, B. L. Gu, S. C. Zhang, K. He, W. Duan, and Y. Xu, *Intrinsic magnetic topological insulators in van der Waals layered MnBi_2Te_4 -family materials*, Sci. Adv. **5**, eaaw5685 (2019).
- [27] M. M. Otrokov, I. I. Klimovskikh, H. Bentmann, D. Estyunin, A. Zeugner, Z. S. Aliev, S. Gaß, A. U. B. Wolter, A. V. Koroleva, A. M. Shikin, M. Blanco-Rey, M. Hoffmann, I. P. Rusinov, A. Y. Vyazovskaya, S. V. Eremeev, Y. M. Koroteev, V. M. Kuznetsov, F. Freyse, J. Sánchez-Barriga, I. R. Amiraslanov, M. B. Babanly, N. T. Mamedov, N. A. Abdullayev, V. N. Zverev, A. Alfonsov, V. Kataev,

- B. Büchner, E. F. Schwier, S. Kumar, A. Kimura, L. Petaccia, G. Di Santo, R. C. Vidal, S. Schatz, K. Kißner, M. Ünzelmann, C. H. Min, S. Moser, T. R. F. Peixoto, F. Reinert, A. Ernst, P. M. Echenique, A. Isaeva, and E. V. Chulkov, *Prediction and observation of an antiferromagnetic topological insulator*, Nature **576**, 416 (2019).
- [28] D. Zhang, M. Shi, T. Zhu, D. Xing, H. Zhang, and J. Wang, *Topological Axion States in the Magnetic Insulator $MnBi_2Te_4$ with the Quantized Magnetoelectric Effect*, Phys. Rev. Lett. **122**, 206401 (2019).
- [29] Y. Deng, Y. Yu, M. Z. Shi, Z. Guo, Z. Xu, J. Wang, X. H. Chen, and Y. Zhang, *Quantum anomalous Hall effect in intrinsic magnetic topological insulator $MnBi_2Te_4$* , Science **367**, 895 (2020).
- [30] W. Ko, M. Kolmer, J. Yan, A. D. Pham, M. Fu, F. Lüpke, S. Okamoto, Z. Gai, P. Ganesh, and A.-P. Li, *Realizing gapped surface states in magnetic topological insulator $MnBi_{2-x}Sb_xTe_4$* , Phys. Rev. B **102**, 115402 (2020).
- [31] F. Lüpke, A. D. Pham, Y. F. Zhao, L. J. Zhou, W. Lu, E. Briggs, J. Bernholc, M. Kolmer, J. Teeter, W. Ko, C. Z. Chang, P. Ganesh, and A. P. Li, *Local manifestations of thickness-dependent topology and edge states in the topological magnet $MnBi_2Te_4$* , Phys. Rev. B **105**, 035423 (2022).
- [32] F. Lüpke, M. Kolmer, J. Yan, H. Chang, P. Vilmercati, H. H. Weitering, W. Ko, and A.-P. Li, in *arXiv2022*.
- [33] P. Li and I. Appelbaum, *Interpreting current-induced spin polarization in topological insulator surface states*, Phys. Rev. B **93**, 220404(R) (2016).
- [34] Y. Zhang, K. He, C. Z. Chang, C. L. Song, L. L. Wang, X. Chen, J. F. Jia, Z. Fang, X. Dai, W. Y. Shan, S. Q. Shen, Q. Niu, X. L. Qi, S. C. Zhang, X. C. Ma, and Q. K. Xue, *Crossover of the three-dimensional topological insulator Bi_2Se_3 to the two-dimensional limit*, Nat. Phys. **6**, 584 (2010).
- [35] See Supplemental Material at [URL will be inserted by publisher] for methods, ARPES characterization, and additional DFT calculations. All files related to a published paper are stored as a single deposit and assigned a Supplemental Material URL. This URL appears in the article's reference list.
- [36] Y. Xia, D. Qian, D. Hsieh, L. Wray, A. Pal, H. Lin, A. Bansil, D. Grauer, Y. S. Hor, R. J. Cava, and M. Z. Hasan, *Observation of a large-gap topological-insulator class with a single Dirac cone on the surface*, Nat. Phys. **5**, 398 (2009).
- [37] Z. Alpichshev, R. R. Biswas, A. V. Balatsky, J. G. Analytis, J. H. Chu, I. R. Fisher, and A. Kapitulnik, *STM imaging of impurity resonances on Bi_2Se_3* , Phys. Rev. Lett. **108**, 206402 (2012).
- [38] N. I. Fedotov and S. V. Zaitsev-Zotov, *Experimental search for one-dimensional edge states at surface steps of the topological insulator Bi_2Se_3 : Distinguishing between effects and artifacts*, Phys. Rev. B **95**, 155403 (2017).
- [39] Y. Xu, G. Jiang, J. Chiu, L. Miao, E. Kotta, Y. Zhang, R. R. Biswas, and L. A. Wray, *Connection topology of step edge state bands at the surface of a three dimensional topological insulator*, New J. Phys. **20**, 073014 (2018).
- [40] Z. Alpichshev, J. G. Analytis, J. H. Chu, I. R. Fisher, and A. Kapitulnik, *STM imaging of a bound state along a step on the surface of the topological insulator Bi_2Te_3* , Phys. Rev. B **84**, 041104(R) (2011).
- [41] Z. Liu, C. X. Liu, Y. S. Wu, W. H. Duan, F. Liu, and J. Wu, *Stable nontrivial Z_2 topology in ultrathin Bi (111) films: A first-principles study*, Phys. Rev. Lett. **107**, 136805 (2011).
- [42] L. Wu, M. Brahlek, R. V. Aguilar, A. V. Stier, C. M. Morris, Y. Lubashevsky, L. S. Bilbro, N. Bansal, S. Oh, and N. P. Armitage, *A sudden collapse in the transport lifetime across the topological phase transition in $(Bi_{1-x}In_x)_2Se_3$* , Nat. Phys. **9**, 410 (2013).
- [43] F. G. Medina, D. Martínez, Á. Díaz-Fernández, F. Domínguez-Adame, L. Rosales, and P. A. Orellana, *Manipulation of Majorana bound states in proximity to a quantum ring with Rashba coupling*, Sci. Rep. **12**, 1071 (2022).
- [44] R. M. Lutchyn, J. D. Sau, and S. Das Sarma, *Majorana fermions and a topological phase transition in semiconductor-superconductor heterostructures*, Phys. Rev. Lett. **105**, 077001 (2010).
- [45] Y. Oreg, G. Refael, and F. von Oppen, *Helical liquids and Majorana bound states in quantum wires*, Phys. Rev. Lett. **105**, 177002 (2010).

Interplay between Topological States and Rashba States as Manifested on Surface Steps at Room Temperature

Wonhee Ko^{1,3†}, Seoung-Hun Kang^{2†}, Jason Lapano², Hao Chang^{1,3}, Jacob Teeter¹, Hoyeon Jeon¹,
Matthew Brahlek², Mina Yoon^{2*}, Robert G. Moore^{2*}, An-Ping Li^{1,3*}

1. Methods

Sample growth of Bi₂Se₃ thin films

Monolayer graphene transferred to 300 nm thermally grown SiO_x on Si substrate were used from commercial vendors (ACS Material). To remove the residual photoresist prior to growth the substrate was first annealed in a flow of forming gas (5% Hydrogen, 95% Nitrogen) at 350 °C for 12 hours [1]. The graphene on Si substrate was then glued to sample plates using silver epoxy and annealed in vacuum at 400 ~ 450 °C for 48 hours prior to growth. After cleaning, samples were transferred to a home-built MBE system operating at a base pressure of $< 5 \times 10^{-10}$ Torr for Bi₂Se₃ deposition. The samples were annealed to 600 °C before growth for a final surface cleaning and to ensure uniformity in growth conditions. Elemental Bi and Se were supplied via thermal effusion cells and fluxes were calibrated using quartz crystal microbalance. Bi was supplied at a flux of 2×10^{13} cm⁻²s⁻¹ and to suppress formation of Se defects, and Se was supplied in excess at a flux of $(10 \sim 20) \times 10^{13}$ cm⁻²s⁻¹. We have followed what is now a standard recipe to produce high quality Bi₂Se₃ films [2,3]. First, we grew an initial 3 QL seed layer at a low temperature (~145 °C). Then, we annealed this buffer layer to a high temperature (~235 °C) slightly below the Bi₂Se₃ desorption, and the films become highly crystalline and flat which serve as an extremely nice template for additional growth to reach the desired thickness. For a 3 QL film, the film was cooled after this annealing up to 235 °C for 15 minutes. For thicker films, after 15 minutes of annealing additional growth has started.

Thickness dependent quality of the film was checked previously by weak antilocalization in transport measurement [4]. The weak antilocalization is extremely sensitive to defects, and the films from the two-step process displayed the signature down to 3 QL.

Angle Resolved Photoemission Spectroscopy

Angle resolved photoemission spectroscopy measurements were performed in a lab-based system coupled to the molecular beam epitaxy system, using a Scienta DA30L hemispherical analyzer with a base pressure of $P < 5 \times 10^{-11}$ mbar and base temperature of $T \sim 8$ K. Samples were illuminated with a VUV He lamp (He-I α = 21.2 eV) light source. For electronic dispersion measurements, a pass energy of 10 eV and 0.5 mm slit was used for a total energy resolution ~ 15 meV and momentum resolution $\sim 0.015 \text{ \AA}^{-1}$.

Scanning tunneling microscopy/spectroscopy.

The STM/STS was taken by Omicron VT-STM operated at ultrahigh vacuum ($< 10^{-10}$ torr) and room temperature. The thin film samples grown in the separate MBE chamber were transferred to the STM chamber by UHV vacuum suitcase ($< 10^{-9}$ torr) to avoid any exposure to the air. The dI/dV spectra were taken by conventional lock-in technique with the modulation voltage of 30 mV and the modulation frequency of 1 kHz. The dI/dV maps were taken in closed-loop mode, where the surface is scanned at certain bias with the current feedback on while the lock-in modulation voltage is applied to measure dI/dV simultaneously.

Density functional theory and tight-binding calculations.

To investigate the electronic properties of Bi₂Se₃ and their terrace structures, we performed *ab initio* calculations based on density functional theory (DFT) [5,6] as implemented in VASP code [7,8]. Projector augmented wave potentials [9] was employed to describe the valence electrons, and the electronic wave functions were expanded by a plane wave basis set with the cutoff energy of 500 eV, and the atomic relaxation was continued until the Hellmann-Feynman force acting on every atom became lower than 0.01 eV/Å. The Perdew-Burke-Ernzerhof (PBE) form [10,11] was employed for the exchange-correlation functional in the generalized gradient approximation (GGA). The Brillouin zone (BZ) was sampled using a 20×20×20 k-grid for the primitive unit cell of Bi₂Se₃. The spin-orbit coupling (SOC) effect is included in

all calculations. These parameters have been thoroughly tested to describe the exact characteristic in the Bi_2Se_3 bulk [12,13]. To investigate electronic properties of the terrace structures, we started by constructing Slater-Koster type tight-binding (TB) model which successfully reproduces the DFT band structure for the Bi_2Se_3 bulk near the Fermi level. Here, we assumed three p orbitals for each Bi and Se atom. Further details of the tight-binding Hamiltonian H in real space are in Supplemental Section 4.

2. ARPES characterization of Bi_2Se_3 thin film samples

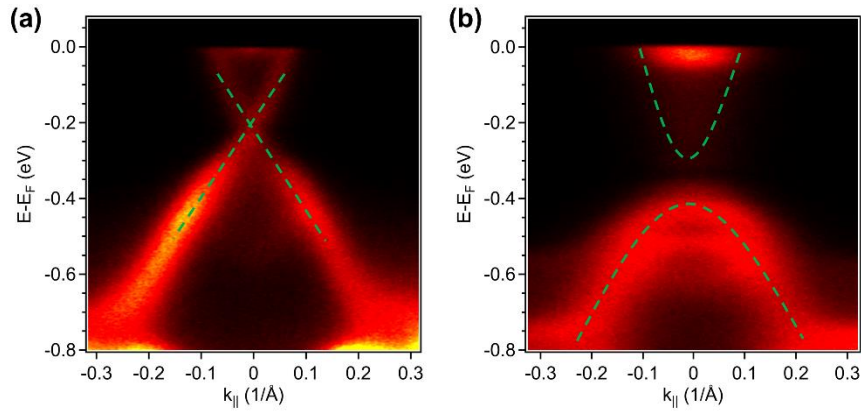


FIG. S1. ARPES on Bi_2Se_3 thin film samples. (a,b) E - k diagram measured by ARPES on 20 QL and 3 QL films, respectively. It is clearly shown that the 20 QL film displays topological surface states with crossing at the Dirac point $E_D \sim -0.3$ eV, but the 3 QL film has a band gap opened in the surface states by interaction between the top and bottom surface states.

3. Large-scale and atomic-scale STM images of Bi_2Se_3 films

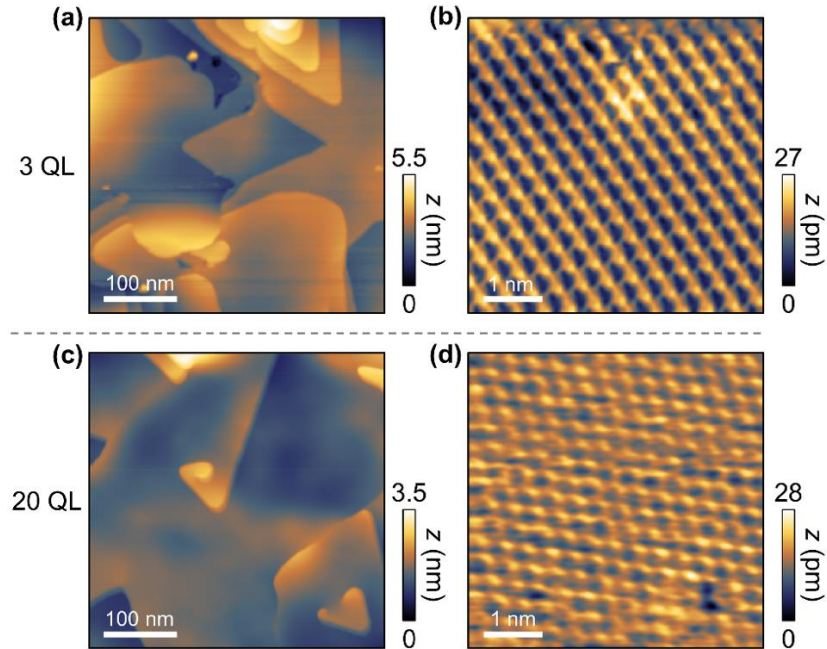


FIG. S2. Large scale and atomic scale topographic images for (a,b) 3 QL film [$V_B = 1$ V, $I = 2$ pA for (a), and $V_B = 0.1$ V, $I = 150$ pA for (b)], and (c,d) 20 QL film [$V_B = 1$ V, $I = 1$ pA for (c), and $V_B = 0.3$ V, $I = 300$ pA for (d)].

4. dI/dV spectra across the step edges for films with various thicknesses, different substrates, and different temperatures

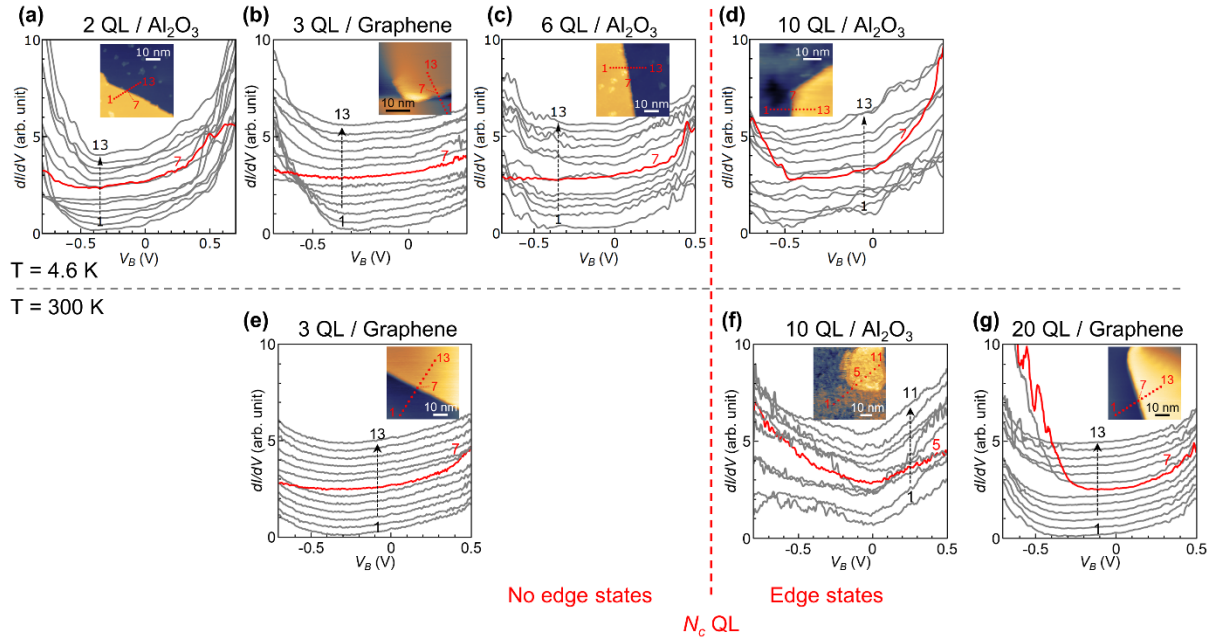


FIG. S3. Summary of dI/dV measurements along the line across the step edges. Top row shows the measurement at $T = 4.6$ K (a-d), and bottom row shows the measurement at room temperature. Film thickness increases from left to right. The critical QL thickness where the edge states appear is at $N_c = 7 \sim 9$.

To estimate the critical QL thickness N_c where the edge states appear and check if other factors affect the edge states appearance, we further measured the Bi_2Se_3 films with various thicknesses (2 ~ 20 QL), different substrates (graphene on SiO_x , Al_2O_3), and temperatures of 4.6 K and room temperature. All STM/S measurements gave the consistent results of disappearance of edge states below 6 QL and appearance of edge states above 10 QL.

5. Normalization of dI/dV maps

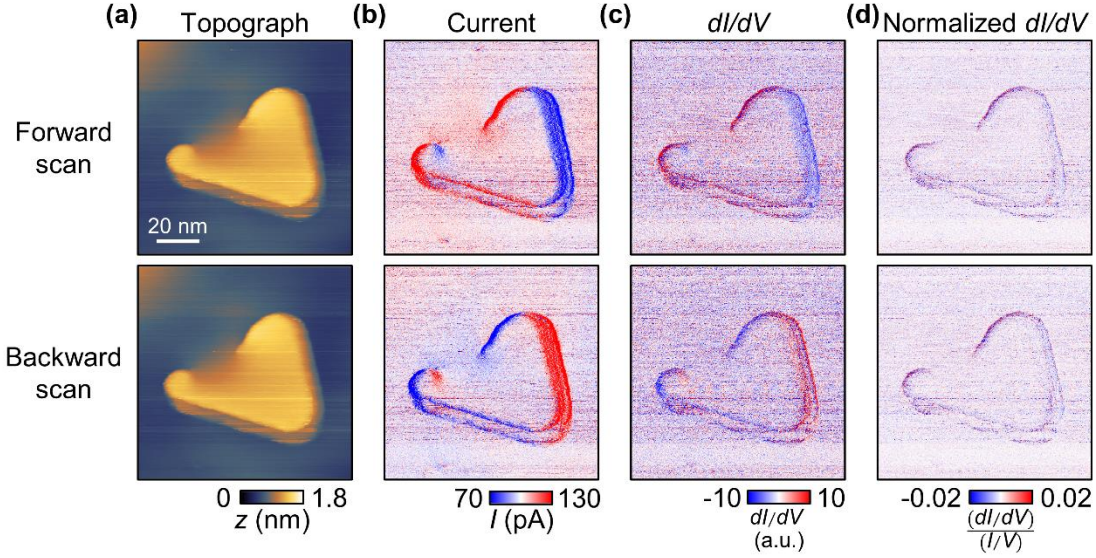


FIG. S4. Normalizing dI/dV maps to compensate current fluctuation. (a-d) Topograph, current, dI/dV , and normalized dI/dV maps, respectively, taken simultaneously on the single QL step ($V = -0.1$ V, $I = 100$ pA). Maps from forward and backward scans are displayed in the top and bottom rows.

In the Fig. 2 of the main text, we plotted normalized dI/dV maps instead of raw dI/dV to compensate the artifact from current fluctuation. Figure S4 shows the topograph, current, dI/dV , and normalized dI/dV maps taken at the same area with the single QL step. Forward and backward scan was acquired at the same time, which displays identical topographs. However, current map shows hysteresis, clearly demonstrated by the inverted current fluctuations at the step for forward and backward scans. The fluctuation in the current is due to the finite feedback speed which makes it unable to retain the constant current when the tip is crossing the steep features and has to retract or extend. Since the tip movement in z direction is opposite for forward and backward scans, current responses are inverted, too. Because dI/dV is proportional not only to the LDOS but also to the total current, fluctuation in the current results in the same fluctuation in dI/dV . As a result, dI/dV maps also display hysteresis at the step edge, which severely hampers the capability to observe the localized edge states. To compensate the effect of current fluctuations, we need to divide dI/dV by I/V ,

and such normalized dI/dV exhibits negligible hysteresis along the step. Therefore, we use the normalized dI/dV to directly visualize the variation of LDOS around the step edges.

6. 2D topological order of Bi_2Se_3

We now provide further discussion of the 2D topological order of the substrate Bi_2Se_3 and the characteristics of the 1D edge state of the nanoribbon located on the substrate.

First, to investigate the 2D topological order of Bi_2Se_3 , we evaluated the Z_2 topological invariant by the Wannier charge center method [14]. The Z_2 index is defined as $Z_2 = \frac{1}{2\pi} [\oint_{\partial B^-} A(\mathbf{k}) - \int_{B^-} F(\mathbf{k})] \text{ mod } 2$, where $A(\mathbf{k}) = i \sum_{n,m \in \text{OCC}} \langle n, \mathbf{k} | \nabla_{\mathbf{k}} | m, \mathbf{k} \rangle$ is Berry connection and $F(\mathbf{k}) = \nabla_{\mathbf{k}} \times A(\mathbf{k}) \cdot \hat{z}$ is the Berry curvature. $Z_2 = 0$ indicates a normal insulator, while $Z_2 = 1$ indicates a topological insulator.

Based on the Z_2 analysis, we confirmed that thin 2D Bi_2Se_3 films with thickness up to 8 QL are not topological insulators, i.e., their Z_2 is 0. Note that this contrasts with Bi thin films [15]. This implies that thin films of Bi_2Se_3 shall not exhibit topological edge states connecting the conduction and valence bands. As a result, our observed 1D edge states cannot be topological edge states of Bi_2Se_3 thin films. As shown in Figs. 3 and 4 in the main text, spin-momentum locking is a prominent feature of both the topological and Rashba states. Therefore, our step edge supports the Rashba state rather than the topological ones, which is also confirmed by the Rashba splitting in the band structures.

7. Tight-binding model for Bi_2Se_3 and the derived topological surface states

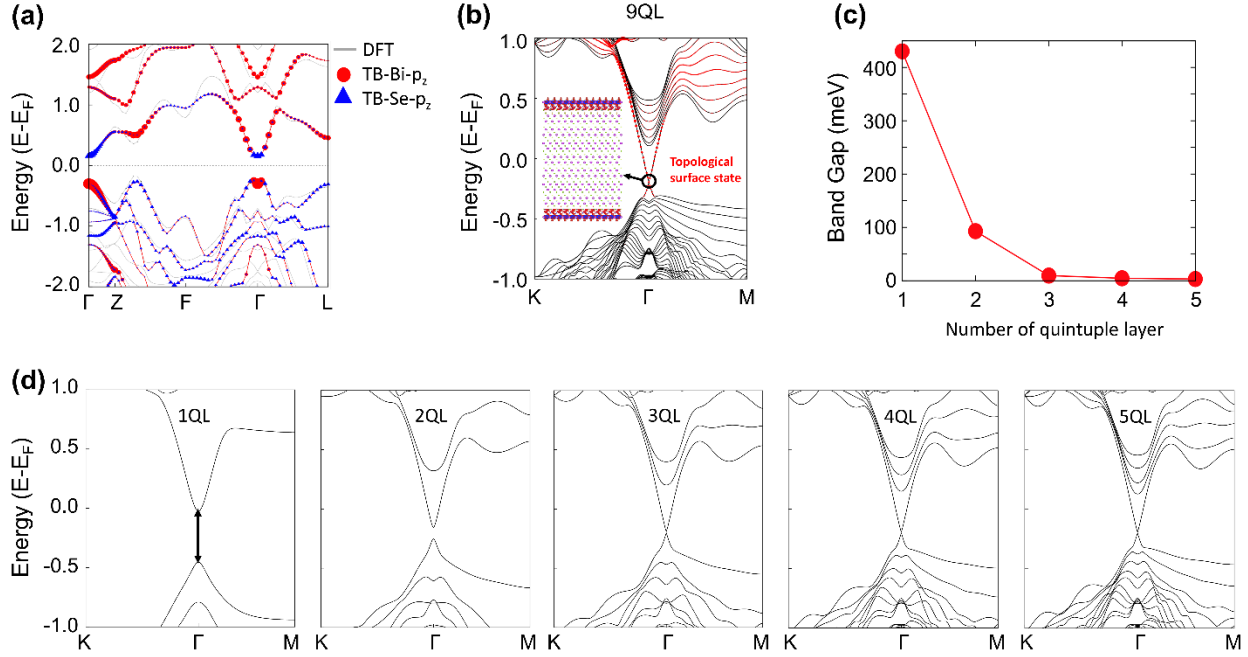


FIG. S5. Tight-binding modeling and topological properties of Bi₂Se₃. (a,b) The band structure of bulk and nine quintuple layers (QL) of Bi₂Se₃, respectively. The grey lines are the DFT bands as a reference, and the red circles and the blue triangles are the tight-binding bands with Bi-P_Z and Se-P_Z orbitals projections, respectively. (c,d) Bandgap, and band structure as a function of Bi₂Se₃ thickness, respectively. It is clearly shown that our tight-binding models describe well the topological properties of Bi₂Se₃, and the films of 5 QL or more layers display topological surface states with Dirac point crossing. However, the films below 5 QL have band gaps opening in the surface states by the interaction between the top and bottom surface states. The band gap increases in size as the decrease of layer thickness.

To investigate the electronic properties of the grain boundaries, we construct a Slater-Koster type TB model which successfully reproduces the DFT based band structure for bulk Bi₂Se₃ near the Fermi level (Fig. S5). We assume three *p*-orbitals per Bi, and Te atom. The tight-binding Hamiltonian *H* in the real space is given as,

$$H = \sum_{\langle i,j \rangle} \sum_{\sigma\alpha\alpha'} [t_{i,j}^{\alpha\alpha'} c_{i\alpha\sigma}^\dagger c_{j\alpha'\sigma} + \text{H.c.}] + H_{SOC},$$

where i, j denotes index for atoms, α, α' for orbitals, and σ for spins, $c_{j\alpha\sigma}$ is an electron annihilation operator and $t_{ij}^{\alpha\alpha'}$ is a transfer matrix, which can be parameterized depending on the direction and distance between a pair of orbitals through the Slater-Koster formula [16]. The H_{SOC} represents the Hamiltonian for the on-site SOC,

$$H_{SOC} = -\lambda_{Bi}\hat{S} \cdot \hat{L}_{Bi} + -\lambda_{Se}\hat{S} \cdot \hat{L}_{Se},$$

where $\lambda_{Bi(Se)}$ is the SOC parameters for Bi (Se) atom, \hat{S} is the spin 1/2 operator, and $\hat{L}_{Bi(Se)}$ is the angular momentum operator of the Bi (Se) atom, respectively [17]. TB parameters are obtained by minimizing the fitness function F,

$$F = \sum_{n,k} \omega_{nk} (E_{TB}^{nk} - E_{DFT}^{nk})^2,$$

where ω_{nk} is the weight for the n -th eigenvalue at \mathbf{k} -point, and $E_{TB(DFT)}^{nk}$ is the eigenvalue obtained by TB (DFT) for bulk Bi_2Se_3 . We use a nonlinear least-squares method based on the Levenberg-Marquardt algorithm [18,19]. Using this procedure, we successfully match the DFT band structure and its topological properties as well as the DFT orbital character for bulk Bi_2Se_3 . The parameters of the tight-binding for Bi_2Se_3 Bulk obtained through the process described above are presented in Table S1. The details of the model structure, calculated using these parameters, are illustrated in Fig. S6.

Table S1. Slater-Koster type tight-binding parameters of Bi_2Se_3 (energies are given in eV).

Bi onsite $u(p_x, p_y, p_z)$: 0.41586827	t of Bi- Se_c pp π : -0.59667815	t of Se_o - Se_o pp π : 0.02795722
Se_c onsite $u(p_x, p_y, p_z)$: -1.09379592	t of Bi- Se_o pp σ : 2.06713581	t of Se_c - Se_o pp σ : -0.17155298
Se_o onsite $u(p_x, p_y, p_z)$: -1.45719560	t of Bi- Se_o pp π : -0.36452264	t of Se_c - Se_o pp π : 0.05732911
t of Bi-Bi pp σ : 0.38783103	t of Se_c - Se_c pp σ : -0.00599293	Bi SOC: 2.06660
t of Bi-Bi pp π : 0.10797423	t of Se_c - Se_c pp π : 0.07808804	Se_c SOC: 0.36320
t of Bi- Se_c pp σ : 1.84617115	t of Se_o - Se_o pp σ : 0.87772499	Se_o SOC: 0.31970

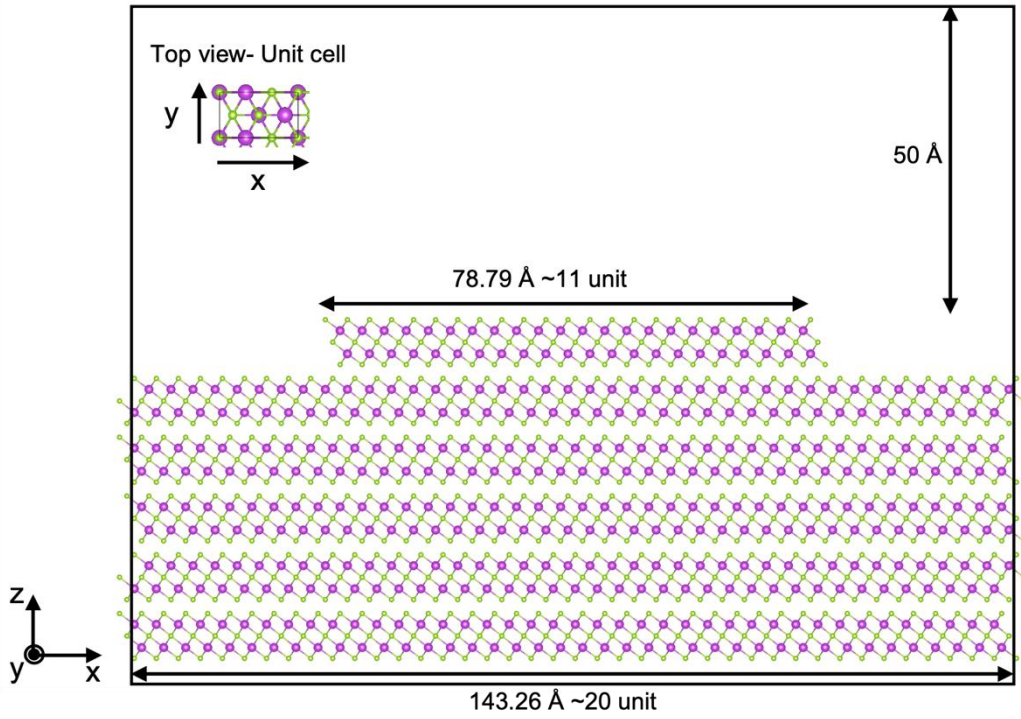


FIG. S6. Our theoretical model structures for step edge on 5 QL- Bi_2Se_3 . Our model system of a nanoribbon on a 5 QL Bi_2Se_3 substrate contains a total of 1113 atoms - the width of the topmost nanoribbon is about 11 unit cells (78.79 Å) and the substrate below the nanoribbon consists of 20 unit cells. In this supercell, the distance between the nanoribbons of neighboring cells is ~ 64.47 Å, and the cell has a vacuum of 50 Å. The area ratio between the nanoribbon and the substrate is 0.55. The dimension of the nanoribbon remains unchanged for different substrates, so on 2 QL Bi_2Se_3 the system contains 513 atoms.

8. The SOC strength dependence of Rashba states

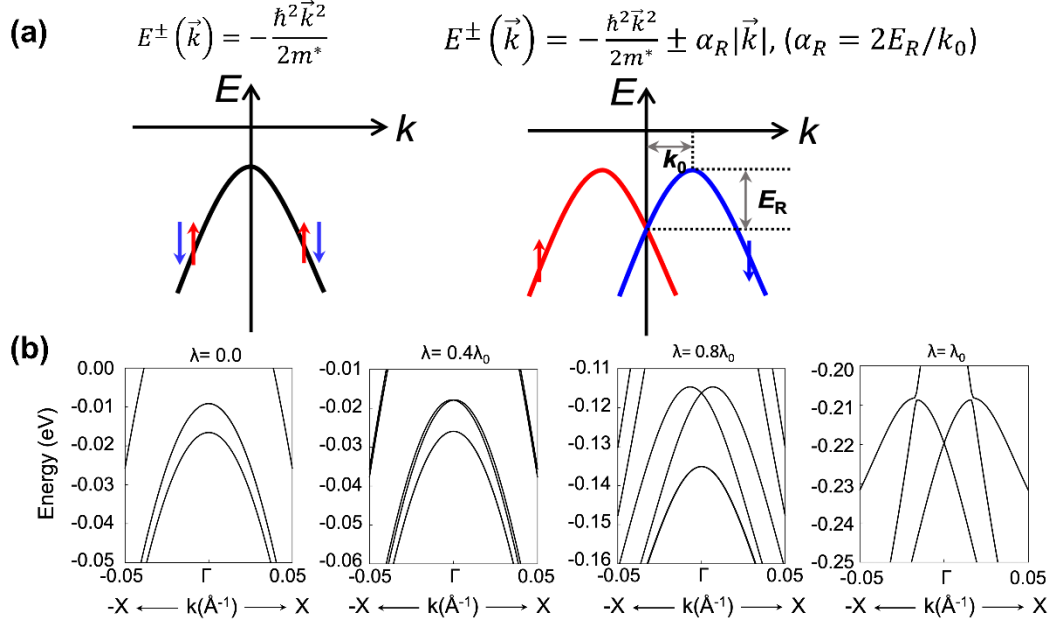


FIG. S7. The strength of Rashba states. (a) The dispersion relation of Rashba states and the definition of Rashba strength ($\alpha_R = 2E_R/k_0$). (b) The evolution of Rashba states as a function of spin-orbit coupling strength for nanoribbon on thick Bi_2Se_3 film (5QL). λ_0 is the SOC strength in the actual material, the nanoribbon on thick Bi_2Se_3 film (5QL). The Rashba state requires band splitting by the inversion symmetry breaking and strong spin-orbit coupling. The strength of Rashba is proportional to the strength of SOC.

9. The 1D Rashba edge states based on the edge shape of the nanoribbon on 5 QL and 2 QL Bi_2Se_3

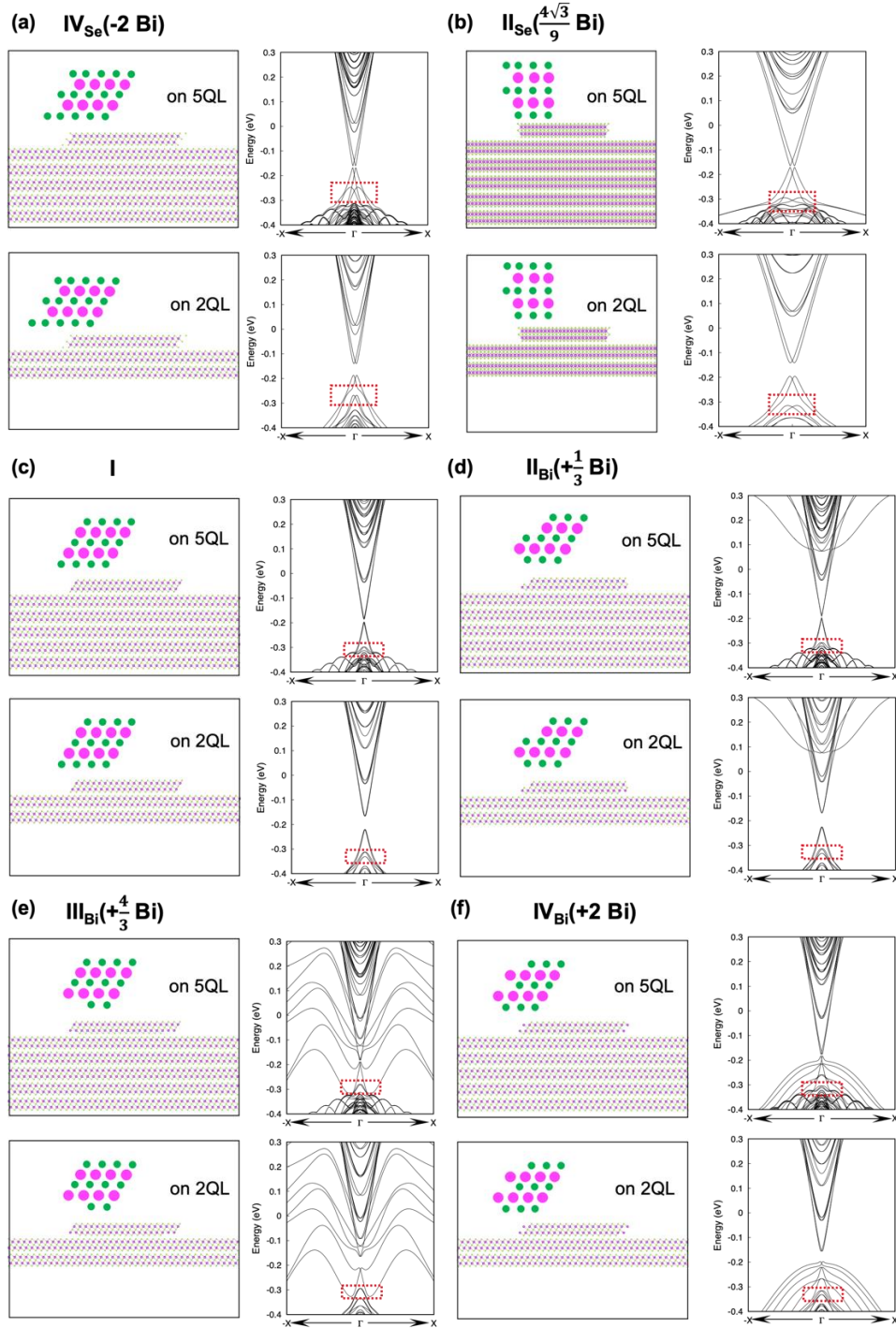


FIG. S8. The edge shape dependence of 1D Rashba states in nanoribbon on 5 QL and 2 QL Bi_2Se_3 .

The structures of stable Bi_2Se_3 nanoribbons were analyzed as a function of the Se chemical potential, and

their edge shapes were determined. Six different structures, ranging from the most Se-rich to Se-poor conditions, were identified and labeled as (a) to (f) [20].

Table S2. The Rashba strength varies for stable edges with different shapes, depending on the Se chemical potential. It is evaluated by equation in Fig. S7 ($\text{eV} \cdot \text{\AA} / 2\pi$).

Stable edge	μ_{Se} (chemical potential of Se)						
	Se-rich	←	I			→	Se-poor
	IV _{Se} (-2 Bi)	III _{Se} (-1 Bi)	II _{Se} ($\frac{4\sqrt{3}}{9}$ Bi)	I	II _{Bi} ($+\frac{1}{3}$ Bi)	III _{Bi} ($+\frac{4}{3}$ Bi)	IV _{Bi} (+2 Bi)
Rashba strength ($\text{eV} \cdot \text{\AA} / 2\pi$)	1.395	1.173	0.641	0.182	0.333	0.275	0.233
Rashba splitting energy (meV)	15	11.3	10	0.4	1	0.7	0.7

We have examined all stable Bi₂Se₃ edge structures reported in the literature [20]. As shown in Fig. 3.2 of the cited ref. [20], the energetics of various Bi₂Se₃ edges depend on the chemical potentials of Se and Bi.

Among these edges, only II_{Se}($\frac{4\sqrt{3}}{9}$ Bi) has an armchair configuration, while the others exhibit different types of zigzag configurations. Regardless of edge type, our study discovered that a 1D Rashba edge state is generated in all structures. The strength of the 1D Rashba edge state varies with the Se chemical potential, as summarized in Table. R2. Under Se-rich condition of our MBE growth, our calculations indicate that the stable edges - IV_{Se}(-2 Bi), III_{Se}(-1Bi, our model structure), and II_{Se}($\frac{4\sqrt{3}}{9}$ Bi) - exhibit strong 1D Rashba edge states. This finding is consistent with our STM/STS measurement.

10. The Rashba states in triangle step edge on 5 QL Bi₂Se₃

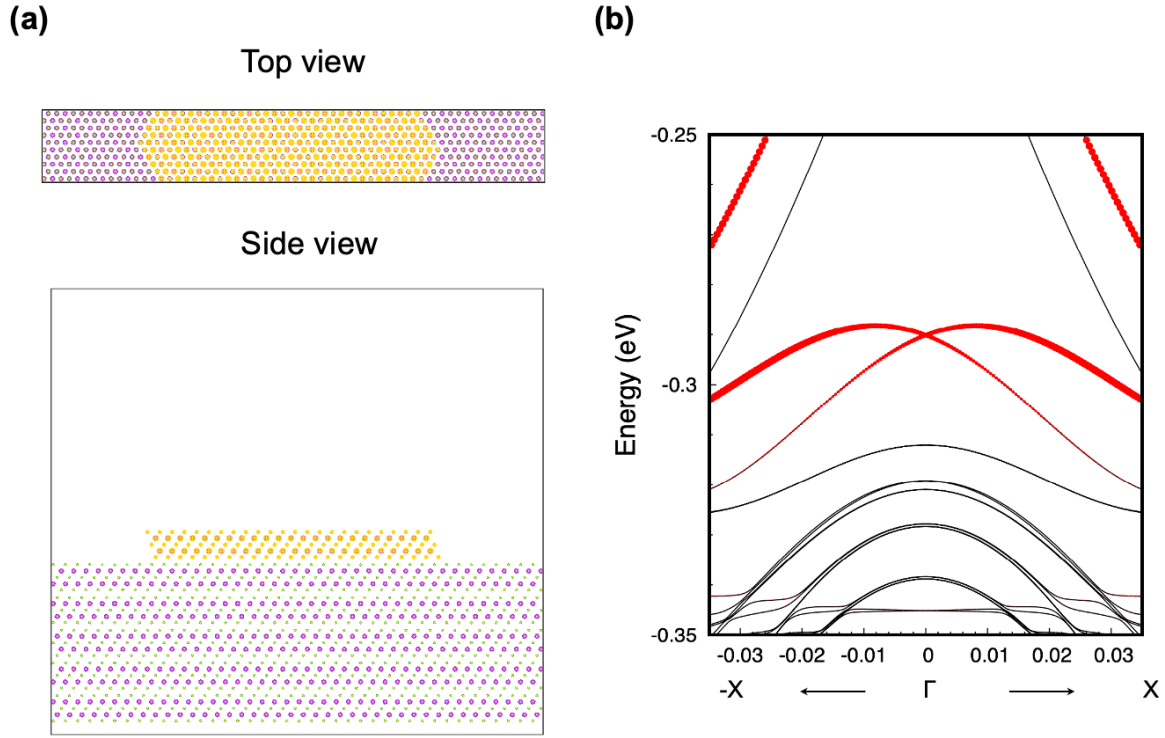


Fig. S9. (a) The atomic structure of the triangle step edge on 5 QL Bi_2Se_3 and (b) its electronic structures.

The electronic structure of a triangularly shaped step edge was indeed examined, as depicted in Fig.S9. The calculation revealed identical Rashba splitting around -0.3 eV, featuring a slightly differing yet comparable Rashba strength ($\sim 0.46 \text{ eV} \cdot \text{\AA}$). Our findings, as outlined in Table S2, suggest that the Rashba strength might fluctuate depending on the edge shape.

11. Consistency of rashba and topological surface states across thick Bi_2Se_3 (≥ 5 QL)

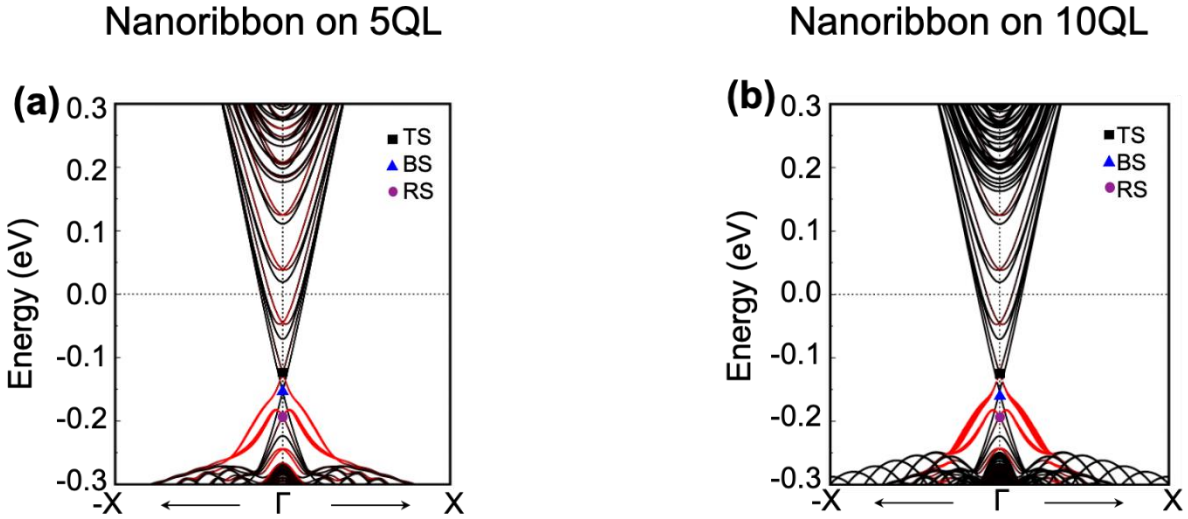


Fig. S10. Electronic band structures of a nanoribbon on (a) 5 QL and (a) 10 QL layers, respectively.

The effect of increasing QL thickness on our results has been carefully considered. Further calculations on a 10 QL film have been carried out and it has been confirmed that our previous observations still hold true. We continue to observe the formation of a 1D Rashba state at the step edges with an almost identical strength, regardless of the thickness ranging from 5 QL to 10 QL, and it coexists with the topological surface states. This phenomenon is demonstrated in Fig. S10. Interestingly, even when the bulk state changes from 5 to 10 QL, the attributes of topological surface states (TS), bottom surface states (BS), and the Rashba state (RS) remain consistent.

References

- [1] J. Xue, J. Sanchez-Yamagishi, D. Bulmash, P. Jacquod, A. Deshpande, K. Watanabe, T. Taniguchi, P. Jarillo-Herrero, and B. J. Leroy, *Scanning tunnelling microscopy and spectroscopy of ultra-flat graphene on hexagonal boron nitride*, Nat. Mater. **10**, 282 (2011).
- [2] N. Bansal, Y. S. Kim, E. Edrey, M. Brahlek, Y. Horibe, K. Iida, M. Tanimura, G. H. Li, T. Feng, H. D. Lee, T. Gustafsson, E. Andrei, and S. Oh, *Epitaxial growth of topological insulator Bi_2Se_3 film on $\text{Si}(111)$ with atomically sharp interface*, Thin Solid Films **520**, 224 (2011).
- [3] M. Brahlek, J. Lapano, and J. S. Lee, *Topological materials by molecular beam epitaxy*, J. Appl. Phys. **128**, 210902 (2020).
- [4] M. Brahlek, N. Koirala, N. Bansal, and S. Oh, *Transport properties of topological insulators: Band bending, bulk metal-to-insulator transition, and weak anti-localization*, Solid State Commun. **215-216**, 54 (2015).
- [5] P. Hohenberg and W. Kohn, *Inhomogeneous electron gas*, Phys. Rev. **136**, B864 (1964).

- [6] W. Kohn and L. J. Sham, *Self-consistent equations including exchange and correlation effects*, Phys. Rev. **140**, A1133 (1965).
- [7] G. Kresse and J. Furthmüller, *Efficient iterative schemes for ab initio total-energy calculations using a plane-wave basis set*, Phys. Rev. B **54**, 11169 (1996).
- [8] G. Kresse, *Ab initio molecular-dynamics for liquid-metals*, Phys. Rev. B **47**, 558 (1993).
- [9] P. E. Blöchl, *Projector augmented-wave method*, Phys. Rev. B **50**, 17953 (1994).
- [10] J. P. Perdew, K. Burke, and M. Ernzerhof, *Generalized Gradient Approximation Made Simple*, Phys. Rev. Lett. **77**, 3865 (1996).
- [11] E. Artacho, D. Sánchez-Portal, P. Ordejón, A. García, and J. M. Soler, *Linear-Scaling ab-initio Calculations for Large and Complex Systems*, Phys. Status Solidi B **215**, 809 (1999).
- [12] Y. Zhang, K. He, C. Z. Chang, C. L. Song, L. L. Wang, X. Chen, J. F. Jia, Z. Fang, X. Dai, W. Y. Shan, S. Q. Shen, Q. Niu, X. L. Qi, S. C. Zhang, X. C. Ma, and Q. K. Xue, *Crossover of the three-dimensional topological insulator Bi_2Se_3 to the two-dimensional limit*, Nat. Phys. **6**, 584 (2010).
- [13] A. Pertsova and C. M. Canali, *Probing the wavefunction of the surface states in Bi_2Se_3 topological insulator: A realistic tight-binding approach*, New J. Phys. **16**, 063022 (2014).
- [14] A. A. Soluyanov and D. Vanderbilt, *Computing topological invariants without inversion symmetry*, Phys. Rev. B **83**, 235401 (2011).
- [15] Z. Liu, C. X. Liu, Y. S. Wu, W. H. Duan, F. Liu, and J. Wu, *Stable nontrivial Z_2 topology in ultrathin Bi (111) films: A first-principles study*, Phys. Rev. Lett. **107**, 136805 (2011).
- [16] J. C. Slater and G. F. Koster, *Simplified LCAO method for the periodic potential problem*, Phys. Rev. **94**, 1498 (1954).
- [17] A. J. Pearce, E. Mariani, and G. Burkard, *Tight-binding approach to strain and curvature in monolayer transition-metal dichalcogenides*, Phys. Rev. B **94**, 155416 (2016).
- [18] K. Levenberg, *A method for the solution of certain non-linear problems in least squares*, Quart. Appl. Math. **2**, 164 (1944).
- [19] D. W. Marquardt, *An Algorithm for least-squares estimation of nonlinear parameters*, SIAM J. Appl. Math. **11**, 432 (1963).
- [20] N. S. Virk, *A Theoretical Investigation of Topological Insulator Nanostructures*, Lausanne, EPFL, 2016.